## PAPER

# Effect of fractal silver electrodes on charge collection and light distribution in semiconducting organic polymer films†

Rachel L. Chamousis,[a] Lilian Chang,[b] William J. Watterson,[c] Rick D. Montgomery,[c] Richard P. Taylor,[c] Adam J. Moule,[b] Sean E. Shaheen,[d] Boaz Ilan,[e] Jao van de Lagemaat[f] and Frank E. Osterloh*[a]

Living organisms use fractal structures to optimize material and energy transport across regions of differing size scales. Here we test the effect of fractal silver electrodes on light distribution and charge collection in organic semiconducting polymer films made of P3HT and PCBM. The semiconducting polymers were deposited onto electrochemically grown fractal silver structures (5000 nm × 500 nm; fractal dimension of 1.71) with PEDOT:PSS as hole-selective interlayer. The fractal silver electrodes appear black due to increased horizontal light scattering, which is shown to improve light absorption in the polymer. According to surface photovoltage spectroscopy, fractal silver electrodes outperform the flat electrodes when the BHJ film thickness is large (>400 nm, 0.4 V photovoltage). Photocurrents of up to 200 microamperes cm$^{-2}$ are generated from the bulk heterojunction (BHJ) photoelectrodes under 435 nm LED (10–20 mW cm$^{-2}$) illumination in acetonitrile solution containing 0.005 M ferrocenium hexafluorophosphate as the electron acceptor. The low IPCE values (0.3–0.7%) are due to slow electron transfer to ferrocenium ion and due to shunting along the large metal–polymer interface. Overall, this work provides an initial assessment of the potential of fractal electrodes for organic photovoltaic cells.

## Introduction

Since the works by Mandelbrodt fractal geometry has been recognized as a universal concept in nature.[1–3] Fractal patterns are not only found in physical objects (*e.g.* clouds and coastlines),[4] and biological structures (trees, neurons, bronchial trees and blood vessels),[5] but also in transient phenomena, including electrical discharge, or social, and economic networks.[6] The pervasiveness of fractal geometry can be understood by considering the advantageous functionality that results from

[a]*Department of Chemistry, University of California, One Shields Avenue, Davis, CA 95616, USA. E-mail: fosterloh@ucdavis.edu; Fax: +1 530 752 8995; Tel: +1 540 754 6242*

[b]*Department of Chemical Engineering and Materials Science, University of California, One Shields Avenue, Davis, CA 95616, USA*

[c]*Department of Physics, University of Oregon, 1585 E. 13th Ave., Eugene, OR 97403, USA*

[d]*Dept. of Electrical, Computer, and Energy Engineering, Department of Physics, Renewable and Sustainable Energy Institute, University of Colorado, UCB 425, Boulder, CO 80309, USA*

[e]*School of Natural Sciences, University of California, 5200 North Lake Road, Merced, CA 95343, USA*

[f]*Chemical and Materials Sciences Center, National Renewable Energy Laboratory, Golden, CO 80401, USA*

† Electronic supplementary information (ESI) available: Electron micrographs of fractal silver electrodes. See DOI: 10.1039/c4ta03204g
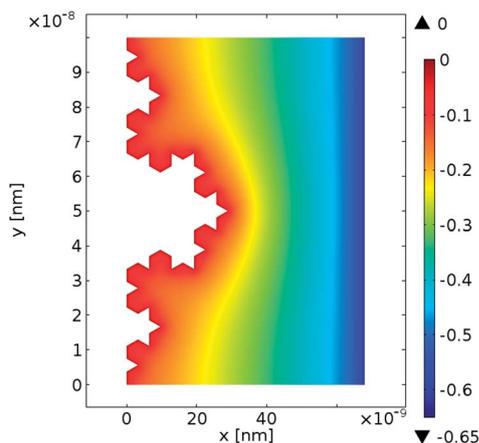
this structure type. By connecting structural patterns over variable size scales with each other, one achieves large surface area and good transport properties. Accordingly, fractal structures are able to efficiently disperse or collect mass, energy, and entropy (information) over large spatial and temporal dimensions. Because of this function, artificial fractal structures have become a subject of fundamental and applied research. Technical applications of fractal structures have now been realized in capacitors and antennas.[7] Potentially, fractals are also well suited to enhance the efficiency of excitonic photovoltaic cells. The basic functions of a solar cell encompass collection of photons (i), conversion into electrical charge and separation of that charge (ii), transport and concentration of electrical charge at their respective electrodes (iii). Branched fractal structures can promote all of these functions. Their network of branches enables them to absorb light over a large cross section and redistribute it *via* scattering (i). The large surface/interface area of the fractal efficiently separates excitons into positive and negative charge carriers (ii). And lastly, the network of connected branches aids transport and concentration of the charge carriers at each electrode (iii). Indeed, theoretical calculations confirm that charge separation and collection can be improved at fractal interfaces. Fig. 1 shows the computed electric potential in a P3HT:PCBM film adjacent to a metallic electrode shaped into a Koch fractal with three levels of iteration. The electric field (the gradient of the potential) outside the electrode is

**16608** | *J. Mater. Chem. A*, 2014, **2**, 16608–16616

This journal is © The Royal Society of Chemistry 2014

**Fig. 1** Computed electric potential (color bar in volts) in a P3HT:PCBM film adjacent to a metallic Koch fractal electrode (enclosed white area). The length of the fractal perimeter is 237 nm. The thickness of the polymer film device is 68 nm. It is illuminated from the right side. The model (see ref. 33) is solved using a finite-element method (COMSOL), and takes into account charge generation, recombination (both Langevin and Shockley–Reed–Hall), transport, and diffusion.

largest where the fractal tip protrudes into the P3HT:PCBM light absorber (center of image). Charge collection will be most efficient in this region. In contrast, a relatively weak electric field is observed in the upper and lower parts of the fractal electrode surface. Here, charge carriers in the polymer film are less attracted to the electrode and charge extraction is slower. These results highlight the importance of 'pointy fractals' with high electric field strength for optimized charge collection.

Even though no experimental studies on fractal solar cells are available yet, there is evidence that structured electrodes can improve charge collection and light harvesting from polymer films.[11–15] For example, the $Fe_2O_3$ electrodes prepared by Kay et al.[16] owe their improved transport properties to their fractal ('cauliflower') structure.[11] Also, Meier et al.[17] found an increase in solar cell efficiency in bulk heterojunction (BHJ) devices resulting from microstructuring PEDOT:PSS and aluminum layers. Here, we use fractal electrodes to promote charge separation and extraction from illuminated P3HT:PCBM BHJ polymer blends.[18–21] Polymer BHJ films are commonly used as light-absorbing layers in organic photovoltaic (OPV) devices,[18,22,23] but their performance is often limited by their ability to absorb long wavelength photons and/or to transport charges to the electrodes.[22,24–26] Both problems can potentially be overcome by using silver fractals as charge collecting electrodes and for improved light distribution. In order to test this hypothesis, we have fabricated the photoelectrode shown in Fig. 2. It consists of a fractal silver layer separated from the P3HT:PCBM light absorber by a PEDOT:PSS hole selective layer. The fractal silver layer on the FTO substrate was made by electrochemical deposition of silver sulfate.[27,28] Deposition under diffusion-limited conditions leads to dendritic silver structures.[27–32] Next, standard spin and drop-coating procedures were used to deposit a PEDOT:PSS hole-selective layer followed by the P3HT:PCBM bulk heterojunction (BHJ) light absorber. Upon illumination, electron hole pairs are

created in the BHJ, and the holes are selectively transported through the PEDOT:PSS layer to be captured at the silver/FTO electrode. Meanwhile the electrons accumulate in the BHJ layer for extraction at the top surface in Fig. 2A. The energetics of this device are shown in Fig. 2B. Theoretically, this photoelectrode can produce an open circuit voltage of 0.7 V, as defined by the work function of PEDOT:PSS and the conduction band of PCBM.

In the following, we employ optical spectroscopy, photo-electrochemistry and surface photovoltage spectroscopy to characterize the device. We find that the silver fractals not only promote charge extraction for thick BHJ layers, but they also enhance horizontal light distribution in the films. However, these benefits are off-set by increased shunting at the enlarged fractal electrode polymer interface. While this work demonstrates the potential of fractal structures for photovoltaic devices, it also highlights the challenge of creating defect-free interfaces for optimum charge separation and low electron–hole recombination.

## Experimental details

### Reagents

Regioregular poly(3-hexylthiophene) (RReg-P3HT) (99.995%), poly(3,4-ethylenedioxythiophene): poly(styrene-sulfonate) (PEDOT: PSS) (2.8 wt% in $H_2O$), ferrocenium hexafluorophosphate
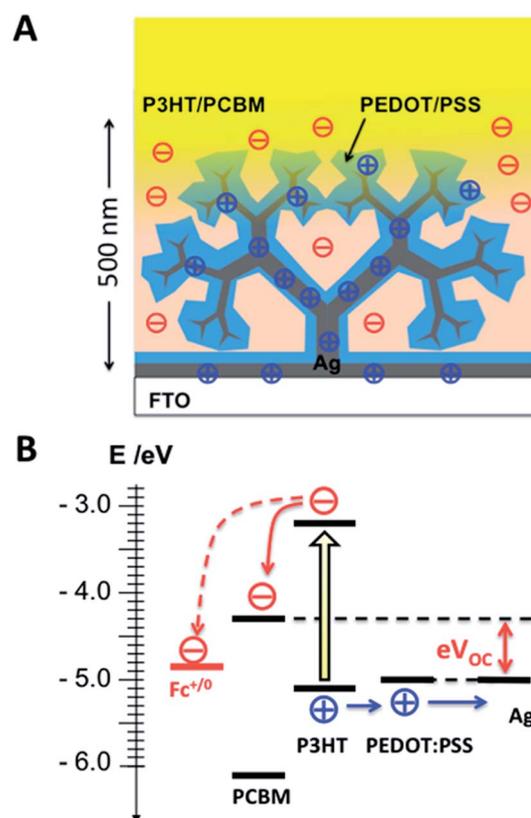


**Fig. 2** (A) Idealized morphology of fractal BHJ device together with charge transport pathways. (B) Energetics in fractal BHJ films. $V_{OC}$ is the theoretical open circuit voltage. $E^0$ for ferrocenium/ferrocene $Fc^{+/0}$ redox couple from ref. 8. Band edges and workfunctions for P3HT/PEDOT:PSS from Berson et al.[9] and for Ag from ref. 10.

(FcPF$_6$) (97.0%), and chlorobenzene (99.8%) were purchased from Aldrich. Ag$_2$SO$_4$ (99.999%) was purchased from Alfa Aesar. H$_2$SO$_4$ (96.4% w/w), acetonitrile (99.8%), and acetone (99.7%) were purchased from Fisher Scientific. K$_2$SO$_4$ (99.9%) was purchased from Mallinckrodt. [6,6]-Phenyl-C61-butyric acid methyl ester (PCBM) (99.5%) was purchased from Nano-C. Tetrabutylammonium hexafluorophosphate (TBAPF$_6$) (>99.0%) was purchased from Fluka Analytical. F:SnO$_2$ (FTO) (TEC 15, 12–14 Ohm sq$^{-1}$) coated glass substrates were purchased from MTI Corporation.

### Flat and fractal Ag electrodes

FTO was initially cleaned by sonication in acetone, methanol, and 2-propanol, followed by ozone/UV treatment. The 100 nm flat silver films on the cleaned FTO were produced by thermal evaporation through a mask. The fractal silver films were electrochemically deposited onto F:SnO$_2$-coated (FTO) glass electrodes connected to a copper wire with a black carbon tape. These electrodes were placed in a solution of 0.005 M Ag$_2$SO$_4$, 0.01 M H$_2$SO$_4$, and 0.5 M Na$_2$SO$_4$ and biased with an applied potential of −1.5 V to −1.6 V *vs.* NHE for five minutes.[27,28] The as-deposited films were immersed in ultrapure water to remove any electrolytes, and carefully washed with acetone to remove the electrode (copper wire/carbon tape) connection.

### BHJ precursor

Solutions of PCBM and RReg-P3HT in chlorobenzene were prepared by adding 10 mg mL$^{-1}$ to 40 mg mL$^{-1}$ of the polymers and by heating to 60 °C in a nitrogen filled glove box for one hour. Once fully dissolved, the two solutions were combined to form the BHJ solution, with a 1 : 1 by mass PCBM:P3HT ratio.

### BHJ/PEDOT:PSS/flat Ag/FTO and BHJ/PEDOT:PSS/fractal Ag/FTO

The flat Ag films were initially placed under nitrogen plasma treatment for 3 s to provide a polar surface for PEDOT:PSS deposition. For flat and fractal Ag, a 40 nm layer of PEDOT:PSS was prepared by spin coating the 2.8 wt% aqueous solution at 2500 rpm for 40 s followed by heating to 110 °C for 3 min. Next, BHJ solutions with increasing concentrations (10 mg mL$^{-1}$ to 40 mg mL$^{-1}$) were deposited by spin-coating onto the PEDOT:PSS layer (2500 rpm to 500 rpm, 30 s to 2 min) to produce BHJ films of increasing thickness, as measured by profilometry (Fig. S2†). The polymer thickness was obtained by subtracting the baseline of the fractal Ag from the baseline of the polymer-coated film. Photoelectrochemical measurements were performed on 1.00 to 1.25 cm$^2$ flat and fractal and BHJ/PEDOT:PSS polymer films on FTO using a three-electrode cell, equipped with a Pt working and a Ag/AgCl reference electrode. The cell electrolyte consisted of 0.005 M FcPF$_6$ and 0.1 M TBAPF$_6$ dissolved in acetonitrile. Acetonitrile was employed as the solvent to avoid dissolution of the PEDOT:PSS layer. Potentials were generated with a Gamry Reference 600 potentiostat controlled by a PC. Photocurrent scans were measured by applying cathodic scans (10 mV s$^{-1}$) with chopped light from a 435 nm Roithner LED (10–20 mW cm$^{-2}$). The curves were calibrated to represent the voltage at zero dark current as the Fc$^{+/0}$ reduction potential. Sample thickness was determined with a Dektak surface profiler calibrated to a Si–SiO$_2$ ellipsometry standard. For surface photovoltage (SPV) spectroscopy measurements, polymer films on silver coated FTO were grounded to a copper plate and transferred into a vacuum chamber containing a vibrating gold Kelvin probe (Besocke Delta Phi, Germany). Each sample was kept under vacuum (10$^{-4}$ mbar) in the dark to remove any adsorbed water from the air. The samples were then illuminated through the probe using light from a 150 W Xe lamp filtered through a Cornerstone 130 monochromator with a 1000 nm blaze grating. Wavelengths were scanned from 0.42 eV to 3.1 eV in increments of 0.01 eV. Diffuse reflectance data were collected using a Thermo Scientific Evolution 220 UV-Vis spectrophotometer equipped with an integrating sphere, and converted to the Kubelka Munk function. SEM samples were imaged with a Philips XL 30 FEG scanning electron microscope. Calculations leading to Fig. 1 were performed using a COMSOL finite-element code of a two-dimensional generalization of the model in Koster *et al.*[33] This model consists of coupled partial differential equations for the electric field potential and the electron and hole densities. It takes into account the charge generation rate of both the electron–hole pairs resulting from the solar illumination throughout the device and of the carriers generated at the surfaces (computed using the effective density of states and Boltzmann thermodynamics). Also considered are Langevin and Shockley–Reed–Hall recombination rates, the applied voltage drop between the right (flat) and left (fractal) electrodes, and the transport and diffusion of the charge carriers and electric field between the electrodes.

## Results and discussion

Scanning electron micrographs of electrodeposited silver structures are shown in Fig. 3. About 50% of the FTO area is covered with spherical silver nanoparticles of 45 nm (±10 nm), while the remaining surface area is covered by the dendritic microstructures of 2–10 micrometer average size and mean height of 0.5 μm, based on SEM and profilometry data (Fig. S1 and S2†). The nanoparticles represent the initial species formed during electrochemical reduction of silver ion in solution. They serve as the seeds for the dendritic microstructures. Nanoparticles found near the stems of the dendrites likely are a result of secondary nucleation. The dendritic structures have a 'fern'-like morphology that consists of a central stem with fine branches extending from the stem, and a subsequent set of hyper-fine branches.

The fractal properties of a representative 'fern' (highlighted in white) are analyzed in Fig. 4A. Clearly, the statistical characteristics of the branches repeat at different size scales, *i.e.* the fern exhibits statistical self-similarity. This repetition is quantified with the fractal dimension $D$ value that can be obtained through a box-counting technique.[34] The $D$ value of the silver dendrite is 1.71. As expected, this value lies between one for a smooth one-dimensional line and two for a two-dimensional plane. By increasing the amount of fine structure in the fractal, it fills more of a 2D plane, and the $D$ value approaches 2. The
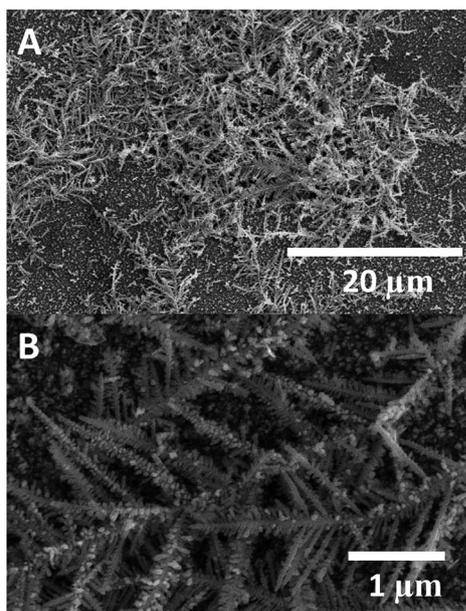
16610 | *J. Mater. Chem. A*, 2014, **2**, 16608–16616

This journal is © The Royal Society of Chemistry 2014

Fig. 3   Scanning electron microscopy images of fractal silver on FTO obtained by electrodeposition at −0.85 V *vs.* NHE for 300 s from an aqueous solution containing 0.005 M $Ag_2SO_4$, 0.01 M $H_2SO_4$, and 0.5 M $Na_2SO_4$.
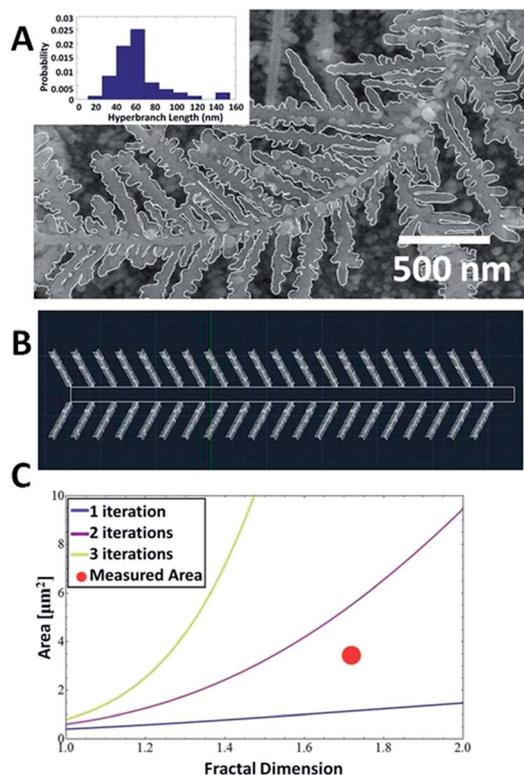


Fig. 4   (A) Scanning electron micrograph of silver fractal (white line emphasized shape). The insert shows the length distribution of the hyperfine branches. (B) Idealized fractal model of the structure in (A). (C) Plot of fractal surface area (measured per 1 μm length of the central stem) as a function of $D$ for fractals with 1, 2, and 3 iterations. The red dot represents the measured area and $D$ for the fractal in (A).

impact of $D$ on the functional properties of the fractal can be demonstrated using the model silver dendrite in Fig. 4B. Matching the physical electrodes, the model features a central stem with fine and hyperfine branches projecting at a characteristic angle of 60°. For simplicity, the model patterns repeat exactly at different size scales (this exact fractal and the statistical fractal of the physical electrode exhibit identical dependencies of their functional properties on $D$ value). Fig. 4C plots the surface area of the model structure as a function of its $D$ value. The plot highlights the increase in surface area obtained by increasing the $D$ value and the number of repeating iterations. The red dot represents the measured $D$ value and surface area of the physical electrode. Note that it lies below the model line for 2 iterations because the hyperfine structure of the physical electrode is not fully formed. The model emphasizes how increasing iteration could affect performance – inclusion of a third iteration would increase the surface area by ~20%, and with it the theoretical charge extraction efficiency.

Fig. 5A and B compare the optical properties of the fractal electrodes with those of flat silver films prepared by physical vapor deposition on FTO. The flat silver film is reflective in the visible and has the appearance of a mirror. In contrast the fractal silver film appears black due to light scattering within the dendritic structures. Accordingly, the diffuse reflectance spectrum of the fractal electrode (solid black line in Fig. 5D) contains a featureless scattering tail reaching from 330 nm (the optical absorption edge of silver) to beyond 900 nm, into the near infrared. Light scattering is not apparent in the spectrum of the flat electrode (black trace in Fig. 5C), where reflection and the silver absorption edge at 320 nm dominate the optical properties.

Significant changes in the spectra occur upon coating the electrodes with PEDOT:PSS/BHJ films (the PEDOT:PSS layers were kept constant at 40 nm). For the 60 and 160 nm thick films the silver absorption edge shifts to 330 and 350 nm respectively. This is due to the increased dielectrical constant of the added polymer film. Similar shifts have been observed before for gold and silver absorption bands.[35–37] In the thicker films, the silver absorption is covered up completely by the absorption of the BHJ layer. That layer contributes absorptions at 450 and 600 nm, due to HOMO–LUMO absorption of P3HT in amorphous and crystalline domains, respectively.[38–41] The diffuse reflectance spectra of the fractal silver electrode are entirely different (Fig. 5D). Here, the initial addition of the polymer increases the reflectivity of the electrode, because of the smoother surface of the added polymer film. As a result, the apparent absorption at 450 nm decreases for the thin films (50 nm and 440 nm). But as the polymer films get thicker (1020 nm and above) this trend reverses, and the absorption is dominated by the 450 nm absorption (HOMO–LUMO of P3HT) as observed for the flat silver film. Notably the absorption of P3HT at 450 nm saturates at ~1000 nm thickness in the fractal film whereas for the flat film, saturation of this absorption requires a thickness of 1300 nm. This suggests that light absorption is improved by the fractal, as explained with the schemes in Fig. 5A and B. While the flat silver electrode favors reflection, the fractal film promotes horizontal light distribution within the film. As a
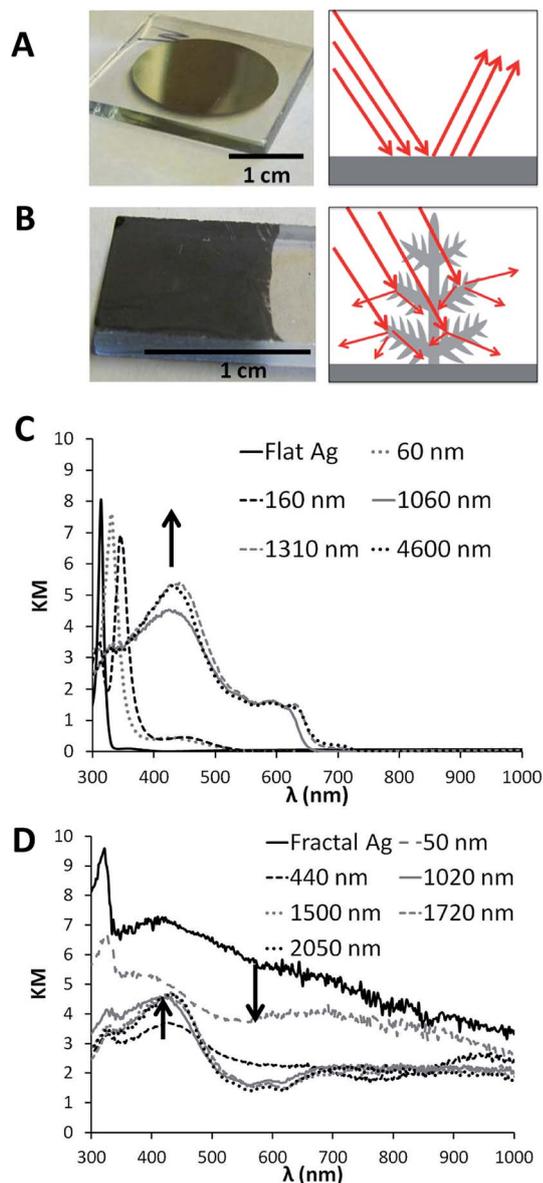
Fig. 5 (A) Flat silver film on FTO from vapor-deposition, (B) fractal silver on FTO from electrodeposition. Diffuse reflectance spectra (Kubelka Munk function) for (C) flat BHJ/PEDOT:PSS Ag/FTO films with varying BHJ thickness, and (D) for fractal BHJ/PEDOT:PSS Ag/FTO. Arrows indicate increasing BHJ layer thickness.

result, light penetration in the polymer layer is increased compared to the flat support. Interestingly, the 600 nm absorption of crystalline P3HT is hardly observable in the fractal film, which indicates that crystallization of P3HT is inhibited by the silver fractals. Neither the flat or fractal BHJ films were thermally annealed, to minimize device damage. Lastly, we note that light scattering from the silver dendrites remains significant at wavelengths above 650 nm, as judged from the absorption spectrum. This lateral light distribution affect could be useful to enhance the absorption for polymers with low light absorption below 1.9 eV.

In order to investigate the ability of the polymer films to generate a photovoltage upon illumination, surface

photovoltage (SPV) spectroscopy was employed. SPV probes the contact potential difference between a reference gold Kelvin probe and a sample film under vacuum.[42] The photovoltage that develops under illumination and as a function of the wavelength of the exciting light provides information about charge separation in inorganic and molecular films.[43–51] SPV spectra recorded for fractal and flat silver PEDOT:PSS/BHJ samples are shown in Fig. 6A. Both contain two positive features (F1 and F2) below and near the bandgap of the blend, and a negative super bandgap feature (F3) at >2.0 eV. According to our previous analysis,[52,53] F1 and F2 are due to excitation of BHJ/PEDOT:PSS interfacial states in the PCBM rich and P3HT-PCBM mixed domains, respectively. The photovoltage arises from polarization of these electron–hole pairs by the built-in field at the PEDOT:PSS\BHJ interface, as shown in Fig. 7B. The built-in field is due to the difference of the BHJ and PEDOT:PSS workfunctions, of 4.7 eV[53] and 5.0 eV,[9] respectively. On the other hand, F3 at 2.0–2.4 eV is assigned to free carriers formed under direct band-gap excitation of crystalline P3HT domains (Fig. 7A). This feature is weaker for the fractal electrode film, due to the lower crystallinity of the polymer layer, as evident from the absence of the 600 nm (2.06 eV) optical absorption. Therefore, the interpretation of the SPV data will focus on F1 and F2, whose combined value can be used as a reporter of the net polarization of charge carriers along the polymer–silver interface. The sum is plotted in Fig. 6B as a function of BHJ film thickness. On flat silver, F1 + F2 first increases with thickness
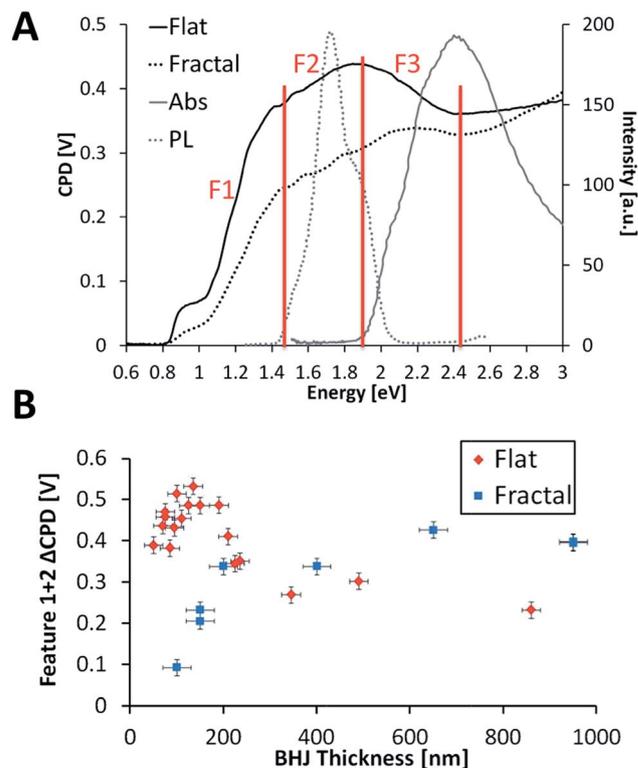


Fig. 6 (A) SPV, absorbance, and PL spectra for flat and fractal BHJ/PEDOT:PSS films on FTO. (B) Variation of features 1 + 2 with BHJ thickness.
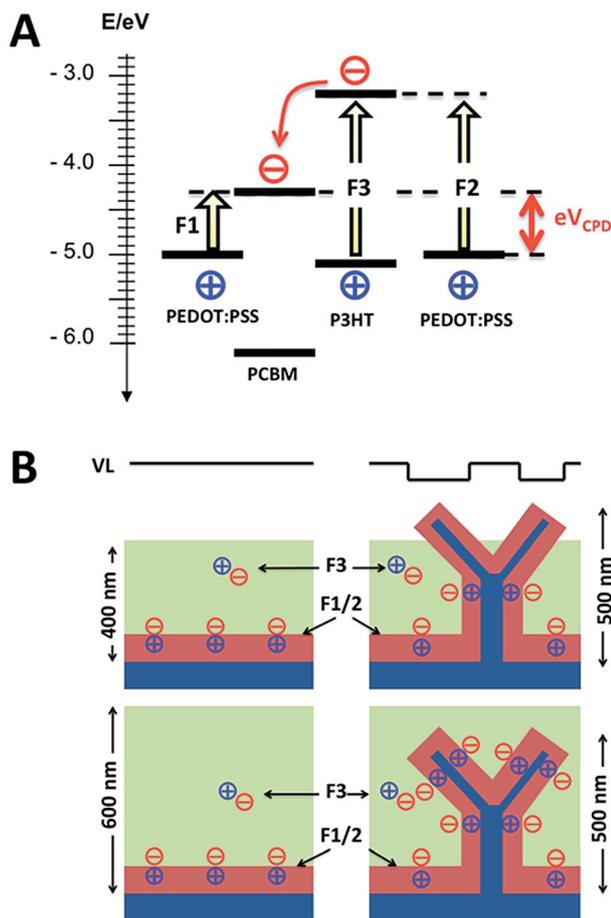
16612 | J. Mater. Chem. A, 2014, 2, 16608–16616

This journal is © The Royal Society of Chemistry 2014

Fig. 7 (A) P3HT-PCBM/PEDOT:PSS energy scheme and assignment of F1−3 photovoltage features. (B) Mechanism of photovoltage generation in thin (<400 nm) and thick BHJ films (>400 nm). In the exposed fractal, in the thin films, the polarization at the BHJ/PEDOT:PSS interface moves the local vacuum level (VL) of the silver fractals to a more oxidizing value. Band edges for P3HT and PEDOT:PSS from Berson et al.[9]

and then decreases to below 0.30 V. The maximum photovoltage value of 0.55 V is reached at about 200 nm film thickness. That corresponds to 79% of the theoretical open circuit voltage (0.7 V) of the device, based on the energy diagram in Fig. 2B. For the fractal electrodes, F1 + F2 is much smaller, but increases monotonically with BHJ thickness. Here, the largest voltage of 0.42 V (60% of the theoretical max) is found above 600 nm, when the polymer film thickness exceeds the average physical height of the fractals (500 nm from profilometry in Fig. S2†). The observed trend can be explained with the scheme in Fig. 7B.

At small BHJ thickness, the 0.5 μm tall silver fractals are partially exposed and stick out towards the Kelvin probe. The exposed silver counteracts the negative polarization of the BHJ film and decreases the observed SPV signal. As the BHJ films become thicker, this 'fractal shunting' becomes less pronounced, and F1 + F2 increase. Eventually F1 + 2 exceeds the values in the flat films, because the interfacial area (which contains F1 and F2 states) in the fractal film is greater than for the flat film, and the number of electron–hole pairs is increased

proportionally. For the flat films, F1 + F2 decreases with thickness because less light reaches the interface due to shading. Overall, the SPV results show that both fractal and flat BHJ films can generate photovoltages of 60 to 78% of the theoretical open circuit voltage of the polymer mixtures, but that shunting from exposed silver structures is a problem when the polymer layer thickness is below the average fractal electrode height. In addition, the larger roughness of the fractals also leads to pin-hole defects in the PEDOT:PSS layer, which further promotes shunting and reduces the photovoltage (see also Discussion below). In order to determine the ability of the BHJ layers to generate photocurrents under illumination, a series of electrochemical measurements was performed on flat and fractal BHJ devices, using ferrocenium ion (Fc$^+$) as sacrificial electron acceptor. Electrochemical scans under chopped illumination from a LED (435 nm, 10–20 mW cm$^{-2}$) are shown in Fig. 8A/B. It can be seen that all films are able to produce cathodic photocurrents at applied potentials negative of the ferrocenium reduction potential $E(Fc^{+/0}) = +0.4$ V $vs.$ NHE.[11] These cathodic photocurrents are in addition to a cathodic dark current from direct electrochemical reduction of the ferrocenium ion. At positive potentials $E_{App} > E(Fc^{+/0})$, small anodic photocurrents from oxidative decomposition of the polymer can be observed. This photocurrent behavior can be explained with the energy diagram in Fig. 2B. Because the Fc$^+$ reduction potential is only 160 mV more reducing than the PEDOT:PSS workfunction, hole extraction at the BHJ–silver interface competes with direct Fc$^+$ reduction when $E_{App} < E(PEDOT:PSS)$. More importantly, no electrical power e$V_{OC}$ can be drawn from the illuminated BHJ photocathode, because that would require an electron acceptor with a reduction potential close to $E_{CB}(PCBM)$. Despite these problems, the device configuration in Fig. 2B allows measurement of photocurrent densities and internal photon to current conversion efficiencies (IPCE) values for both fractal and flat polymer films. Compared to typical BHJ devices,[54] experimental IPCE values for the photoelectrochemical device here (Fig. 8C) are below 2.5%. The reason for these low values is that charge transfer is limited by the kinetics of Fc$^+$ reduction at the BHJ–electrolyte interface and by competitive light absorption at 450 nm from the ferrocenium reagent.[26]

Values for the flat silver films are 1.7% for the thinnest films, then go up to 2.2% for the 220 nm BHJ film, and then decrease to 2.0% for the 650 nm film. This points to light absorption problems in the thinnest and charge transport problems in the thickest film, in agreement with the literature.[18–21,55,56] The IPCE values for the fractal films are lower (0.3–0.7%), but here the highest values are observed for the thickest films. This suggests that the silver fractals do indeed promote charge extraction, but that the photoelectrochemical performance is limited by shunting at the silver–polymer interface, as already seen in the SPV results. The silver–polymer interface is much larger than for the flat silver devices – this makes it more prone to interfacial defects that cause recombination. In addition, shunting may occur due to incomplete coverage of the fractal silver branches with PEDOT:PSS. Lastly, we cannot rule out that some of the performance variations between fractal and flat devices are due to changes in P3HT:PCBM morphology, as they could result
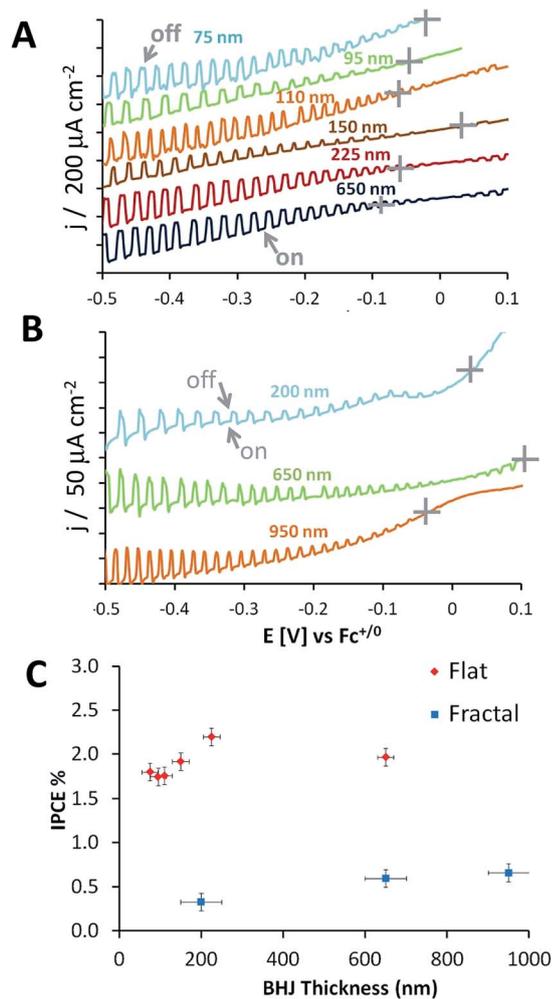
This journal is © The Royal Society of Chemistry 2014

J. Mater. Chem. A, 2014, 2, 16608–16616 | 16613

**Fig. 8** Photoelectrochemical data for BHJ/PEDOT:PSS films on (A) flat and (B) fractal silver electrodes, as a function of BHJ thickness. Conditions: 0.01 M $(Bu_4N)PF_6$, 0.005 M $FcBF_4$ in $CH_3CN$ using 435 nm LED (10–20 mW $cm^{-2}$). Potentials are reported *versus* the $Fc^{+/0}$ potential of +0.4 V (*vs.* NHE). Cross-bars indicate zero current. (C) Incident photon to current efficiencies (IPCE%) *versus* active layer thickness.

from the difference in electrode structure, and from the resulting differences in deposition parameters, including coating speed and solvent evaporation rate.[57]

## Conclusion

In summary, we present the first evaluation of a fractal electrode to extract charge from a polymer bulk heterojunction. The fractal electrode increases light absorption in the polymer due to horizontal light distribution throughout the film, especially at short wavelengths, where the scattering power is strongest. This optical enhancement is not significant for P3HT, due to its short light penetration depth of 200 nm, but it could be useful to increase light penetration in other, less strongly absorbing polymers. The fractal electrode also improves charge extraction for thick polymer films, as observed in the higher photovoltage value for the >500 nm BHJ films, and in the increasing

photocurrents measured for the 650 and 950 nm polymer films. This effect is due to the combination of higher interfacial area and better electronic connectivity in the fractals. At the same time, the fractal electrodes suffer from higher electron–hole recombination, caused by the increased area of the silver–polymer interface. Improved performance may be achievable if ways to reduce shunting at the fractal-light absorber interface can be found, and methods to grow more homogeneous silver films with higher fractal coverage and smaller structure size (<500 nm) can be developed.

## Acknowledgements

## Notes and references

1 D. Avnir, *The fractal approach to heterogeneous chemistry: surfaces, colloids, polymers*, Wiley, Chichester, 1989, p xvii, p. 441.

2 L. Nottale, Scale relativity and fractal space-time: a new approach to unifying relativity and quantum mechanics, *Distributed by World Scientific: London Singapore*, Imperial College Press, Hackensack, NJ, 2011, p xxi, p. 742.

3 R. P. Taylor, Artificial Vision: Vision of Beauty, *Phys. World*, 2011, 22–27.

4 B. Mandelbrot, How Long Is Coast of Britain – Statistical Self-Similarity and Fractional Dimension, *Science*, 1967, **156**(3775), 636–638.

5 J. Bassingthwaighte, L. S. Liebovitch and B. J. West, *Fractal Physiology*, Oxford University Press, Oxford, 1994.

6 B. Mandelbrot, The Variation of Certain Speculative Prices, *J. Bus.*, 1963, **36**(4), 394–419.

7 R. G. Hohlfeld and N. Cohen, Self-similarity and the geometric requirements for frequency independence in antennae, *Fractals*, 1999, **7**, 79–84.

8 N. G. Connelly and W. E. Geiger, Chemical redox agents for organometallic chemistry, *Chem. Rev.*, 1996, **96**(2), 877–910.

9 S. Berson, R. de Bettignies, S. Bailly, S. Guillerez and B. Jousselme, Elaboration of P3HT/CNT/PCBM composites for organic photovoltaic cells, *Adv. Funct. Mater.*, 2007, **17**(16), 3363–3370.

10 D. R. Lide, Electron Work Function of the Elements, in *CRC Handbook of Chemistry and Physics, 88 (Internet Version 2008)*, CRC Press/Taylor and Francis, Boca Raton, FL, 2008.

11 F. E. Osterloh, Inorganic Nanostructures for Photoelectrochemical and Photocatalytic Water Splitting, *Chem. Soc. Rev.*, 2013, **42**(6), 2294–2320.

12 F. Ramiro-Manzano, P. Atienzar, I. Rodriguez, F. Meseguer, H. Garcia and A. Corma, Apollony photonic sponge based photoelectrochemical solar cells, *Chem. Commun.*, 2007, 242–244.

13  A. Provata, P. Falaras and A. Xagas, Fractal features of titanium oxide surfaces, *Chem. Phys. Lett.*, 1998, **297**(5–6), 484–490.

14  T. Stergiopoulos, I. M. Arabatzis, H. Cachet and P. Falaras, Photoelectrochemistry at $SnO_2$ particulate fractal electrodes sensitized by a ruthenium complex – solid-state solar cell assembling by incorporating a composite polymer electrolyte, *J. Photochem. Photobiol., A*, 2003, **155**(1–3), 163–170.

15  M. Koehler, C. D. Canestraro, M. C. Schnitzler, M. M. Oliveira, A. J. G. Zarbin, L. S. Roman and M. G. E. Da Luz, Evidence of fractal structure for charge transport in carbon-nanotube/conjugated-polymer composites, *EPL*, 2007, **79**(4), 47011.

16  A. Kay, I. Cesar and M. Gratzel, New benchmark for water photooxidation by nanostructured alpha-$Fe_2O_3$ films, *J. Am. Chem. Soc.*, 2006, **128**(49), 15714–15721.

17  R. Meier, C. Birkenstock, C. M. Palumbiny and P. Muller-Buschbaum, Efficiency-improved organic solar cells based on plasticizer assisted soft embossed PEDOT: PSS layers, *Phys. Chem. Chem. Phys.*, 2012, **14**(43), 15088–15098.

18  A. C. Mayer, S. R. Scully, B. E. Hardin, M. W. Rowell and M. D. McGehee, Polymer-based solar cells, *Mater. Today*, 2007, **10**(11), 28–33.

19  F. Padinger, R. S. Rittberger and N. S. Sariciftci, Effects of Postproduction Treatment on Plastic Solar Cells, *Adv. Funct. Mater.*, 2003, **13**(1), 85–88.

20  W. Ma, C. Yang, X. Gong, K. Lee and A. J. Heeger, Thermally Stable, Efficient Polymer Solar Cells with Nanoscale Control of the Interpenetrating Network Morphology, *Adv. Funct. Mater.*, 2005, **15**(10), 1617–1622.

21  M. Reyes-Reyes, K. Kim, J. Dewald, R. López-Sandoval, A. Avadhanula, S. Curran and D. L. Carroll, Meso-Structure Formation for Enhanced Organic Photovoltaic Cells, *Org. Lett.*, 2005, **7**(26), 5749–5752.

22  D. Carsten and D. Vladimir, Polymer–fullerene bulk heterojunction solar cells, *Rep. Prog. Phys.*, 2010, **73**(9), 096401.

23  N. S. Sariciftci, L. Smilowitz, A. J. Heeger and F. Wudl, Photoinduced Electron Transfer from a Conducting Polymer to Buckminsterfullerene, *Science*, 1992, **258**(5087), 1474–1476.

24  A. Foertig, A. Wagenpfahl, T. Gerbich, D. Cheyns, V. Dyakonov and C. Deibel, Nongeminate Recombination in Planar and Bulk Heterojunction Organic Solar Cells, *Adv. Energy Mater.*, 2012, **2**(12), 1483–1489.

25  L. J. A. Koster, S. E. Shaheen and J. C. Hummelen, Pathways to a New Efficiency Regime for Organic Solar Cells, *Adv. Energy Mater.*, 2012, **2**(10), 1246–1253.

26  J. D. Servaites, M. A. Ratner and T. J. Marks, Organic solar cells: a new look at traditional models, *Energy Environ. Sci.*, 2011, **4**(11), 4410–4422.

27  P. Carro, S. Ambrosolio, S. L. Marchiano, A. H. Creus, R. C. Salvarezza and A. J. Arvia, Transport phenomena and growth modes of silver electrodeposits, *J. Electroanal. Chem.*, 1995, **396**(1–2), 183–195.

28  X. Qin, Z. Miao, Y. Fang, D. Zhang, J. Ma, L. Zhang, Q. Chen and X. Shao, Preparation of Dendritic Nanostructures of Silver and Their Characterization for Electroreduction, *Langmuir*, 2012, **28**(11), 5218–5226.

29  K. Sreejith, J. Nuwad, C. Thinaharan, G. K. Dey and C. G. S. Pillai, Electrodeposition of silver nanodendrites, *Nanotechnology*, 2007, **18**(12), 125610.

30  E. Ben-Jacob and P. Garik, The formation of patterns in non-equilibrium growth, *Nature*, 1990, **343**(6258), 523–530.

31  Q. Zhou, S. Wang, N. Jia, L. Liu, J. Yang and Z. Jiang, Synthesis of highly crystalline silver dendrites microscale nanostructures by electrodeposition, *Mater. Lett.*, 2006, **60**(29–30), 3789–3792.

32  A. P. Alivisatos, Naturally Aligned Nanocrystals, *Science*, 2000, **289**(5480), 736–737.

33  L. J. A. Koster, E. C. P. Smits, V. D. Mihailetchi and P. W. M. Blom, Device model for the operation of polymer/fullerene bulk heterojunction solar cells, *Phys. Rev. B: Condens. Matter Mater. Phys.*, 2005, **72**(8), 085205–085213.

34  M. S. Fairbanks and R. P. Taylor, Scaling Analysis of Spatial and Temporal Patterns: From the Human Eye to the Foraging Albatross, in *Non-linear Dynamical Analysis for the Behavioral Sciences Using Real Data*, Taylor and Francis Group, Boca Raton, 2011.

35  D. D. Evanoff, R. L. White and G. Chumanov, Measuring the distance dependence of the local electromagnetic field from silver nanoparticles, *J. Phys. Chem. B*, 2004, **108**(5), 1522–1524.

36  J. Wang, Y. J. Lee, A. S. Chadha, J. Yi, M. L. Jespersen, J. J. Kelley, H. M. Nguyen, M. Nimmo, A. V. Malko, R. A. Vaia, W. D. Zhou and J. W. P. Hsu, Effect of Plasmonic Au Nanoparticles on Inverted Organic Solar Cell Performance, *J. Phys. Chem. C*, 2013, **117**(1), 85–91.

37  F. Osterloh, H. Hiramatsu, R. Porter and T. Guo, Alkanethiol-Induced Structural Rearrangements in Silica-Gold Core-Shell-type Nanoparticle Clusters: An Opportunity for Chemical Sensor Engineering, *Langmuir*, 2004, **20**(13), 5553–5558.

38  P. Vanlaeke, A. Swinnen, I. Haeldermans, G. Vanhoyland, T. Aernouts, D. Cheyns, C. Deibel, J. D'Haen, P. Heremans, J. Poortmans and J. V. Manca, P3HT/PCBM bulk heterojunction solar cells: Relation between morphology and electro-optical characteristics, *Sol. Energy Mater. Sol. Cells*, 2006, **90**(14), 2150–2158.

39  D. Chirvase, J. Parisi, J. C. Hummelen and V. Dyakonov, Influence of nanomorphology on the photovoltaic action of polymer–fullerene composites, *Nanotechnology*, 2004, **15**(9), 1317.

40  V. Shrotriya, J. Ouyang, R. J. Tseng, G. Li and Y. Yang, Absorption spectra modification in poly(3-hexylthiophene):methanofullerene blend thin films, *Chem. Phys. Lett.*, 2005, **411**(1–3), 138–143.

41  W. C. Tsoi, S. J. Spencer, L. Yang, A. M. Ballantyne, P. G. Nicholson, A. Turnbull, A. G. Shard, C. E. Murphy, D. D. C. Bradley, J. Nelson and J. S. Kim, Effect of Crystallization on the Electronic Energy Levels and Thin

Film Morphology of P3HT: PCBM Blends, *Macromolecules*, 2011, **44**(8), 2944–2952.

42 L. Kronik and Y. Shapira, Surface photovoltage phenomena: theory, experiment, and applications, *Surf. Sci. Rep.*, 1999, **37**(1–5), 1–206.

43 C. M. Aldao, G. D. Waddill, P. J. Benning, C. Capasso and J. H. Weaver, Photovoltaic effects in temperature-dependent Fermi-level movement for GaAs(110), *Phys. Rev. B: Condens. Matter Mater. Phys.*, 1990, **41**(9), 6092–6095.

44 B. L. Sharma, *Metal-Semiconductor Schottky Barrier Junctions and Their Applications*, Springer-Verlag, New York, 2013, p. 386.

45 S. Bastide, R. Butruille, D. Cahen, A. Dutta, J. Libman, A. Shanzer, L. Sun and A. Vilan, Controlling the Work Function of GaAs by Chemisorption of Benzoic Acid Derivatives, *J. Phys. Chem. B*, 1997, **101**(14), 2678–2684.

46 M. Bruening, R. Cohen, J. F. Guillemoles, T. Moav, J. Libman, A. Shanzer and D. Cahen, Simultaneous Control of Surface Potential and Wetting of Solids with Chemisorbed Multifunctional Ligands, *J. Am. Chem. Soc.*, 1997, **119**(24), 5720–5728.

47 R. Cohen, N. Zenou, D. Cahen and S. Yitzchaik, Molecular electronic tuning of Si surfaces, *Chem. Phys. Lett.*, 1997, **279**(5–6), 270–274.

48 R. Cohen, S. Bastide, D. Cahen, J. Libman, A. Shanzer and Y. Rosenwaks, Controlling surfaces and interfaces of semiconductors using organic molecules, *Opt. Mater.*, 1998, **9**(1–4), 394–400.

49 I. H. Campbell, S. Rubin, T. A. Zawodzinski, J. D. Kress, R. L. Martin, D. L. Smith, N. N. Barashkov and J. P. Ferraris, Controlling Schottky energy barriers in organic electronic devices using self-assembled monolayers, *Phys. Rev. B: Condens. Matter Mater. Phys.*, 1996, **54**(20), R14321–R14324.

50 I. M. Dharmadasa, G. G. Roberts and M. C. Petty, Cadmium telluride/Langmuir film photovoltaic structures, *Electron. Lett.*, 1980, **16**(6), 201–202.

51 R. Cohen, S. Bastide, D. Cahen, J. Libman, A. Shanzer and Y. Rosenwaks, Controlling electronic properties of CdTe by adsorption of dicarboxylic acid derivatives: relating molecular parameters to band bending and electron affinity changes, *Adv. Mater.*, 1997, **9**(9), 746–749.

52 F. E. Osterloh, M. A. Holmes, L. Chang, A. J. Moule and J. Zhao, Photochemical charge separation in poly(3-hexylthiophene) (P3HT) films observed with surface photovoltage spectroscopy, *J. Phys. Chem. C*, 2013, **117**(51), 26905–26913.

53 F. E. Osterloh, M. A. Holmes, J. Zhao, L. Chang, S. Kawula, J. D. Roehling and A. J. Moulé, P3HT: PCBM Bulk-Heterojunctions: Observing Interfacial and Charge Transfer States with Surface Photovoltage Spectroscopy, *J. Phys. Chem. C*, 2014, **118**(27), 14723–14731.

54 B. A. Collins, J. R. Tumbleston and H. Ade, Miscibility, Crystallinity, and Phase Development in P3HT/PCBM Solar Cells: Toward an Enlightened Understanding of Device Morphology and Stability, *J. Phys. Chem. Lett.*, 2011, **2**(24), 3135–3145.

55 S. van Bavel, E. Sourty, G. de With, K. Frolic and J. Loos, Relation between Photoactive Layer Thickness, 3D Morphology, and Device Performance in P3HT/PCBM Bulk-Heterojunction Solar Cells, *Macromolecules*, 2009, **42**(19), 7396–7403.

56 R. A. J. Janssen, J. C. Hummelen and N. S. Sariciftci, Polymer–Fullerene Bulk Heterojunction Solar Cells, *MRS Bull.*, 2005, **30**(01), 33–36.

57 M. A. Ruderer, S. Guo, R. Meier, H. Y. Chiang, V. Korstgens, J. Wiedersich, J. Perlich, S. V. Roth and P. Muller-Buschbaum, Solvent-Induced Morphology in Polymer-Based Systems for Organic Photovoltaics, *Adv. Funct. Mater.*, 2011, **21**(17), 3382–3391.